Statistics of Cloud Optical Properties from Airborne Lidar Measurements

JOHN E. YORKS, DENNIS L. HLAVKA, AND WILLIAM D. HART

Science Systems and Applications, Inc., Lanham, Maryland

MATTHEW J. MCGILL

NASA Goddard Space Flight Center, Greenbelt, Maryland

(Manuscript received 15 June 2010, in final form 13 January 2011)

ABSTRACT

Accurate knowledge of cloud optical properties, such as extinction-to-backscatter ratio and depolarization ratio, can have a significant impact on the quality of cloud extinction retrievals from lidar systems because parameterizations of these variables are often used in nonideal conditions to determine cloud phase and optical depth. Statistics and trends of these optical parameters are analyzed for 4 yr (2003–07) of cloud physics lidar data during five projects that occurred in varying geographic locations and meteorological seasons. Extinction-to-backscatter ratios (also called lidar ratios) are derived at 532 nm by calculating the transmission loss through the cloud layer and then applying it to the attenuated backscatter profile in the layer, while volume depolarization ratios are computed using the ratio of the parallel and perpendicular polarized 1064-nm channels. The majority of the cloud layers yields a lidar ratio between 10 and 40 sr, with the lidar ratio frequency distribution centered at 25 sr for ice clouds and 16 sr for altocumulus clouds. On average, for ice clouds the lidar ratio slightly decreases with decreasing temperature, while the volume depolarization ratio increases significantly as temperatures decrease. Trends for liquid water clouds (altocumulus clouds) are also observed. Ultimately, these observed trends in optical properties, as functions of temperature and geographic location, should help to improve current parameterizations of extinction-to-backscatter ratio, which in turn should yield increased accuracy in cloud optical depth and radiative forcing estimates.

1. Introduction

Clouds have a significant influence on the earth's radiation budget (Rajeevan and Srinivasan 2000; Stephens 2005; Yorks et al. 2009). Obtaining an accurate assessment of these cloud effects on the atmospheric radiation budget remains a major challenge in understanding and predicting the climate system (Solomon et al. 2007). To improve cloud parameterizations in global climate models, a global climatology of both ice and liquid water clouds that includes information about their optical and physical properties is necessary. A combination of both in situ and remote sensing measurements is necessary for this climatology, because remote sensing instruments can provide global data in remote regions with high temporal and spatial resolution that are not accessible using in situ measurements (Wang and Sassen 2001). The launches of the Geoscience Laser Altimeter System (GLAS; Spinhirne et al. 2005) in January 2003 and the Cloud–Aerosol Lidar and Infrared Pathfinder Satellite Observations (CALIPSO; Winker et al. 2009a) project in April 2006 have allowed the scientific community to investigate global statistics of optically thin cirrus cloud optical properties to the limit of signal attenuation.

Ground-based and airborne elastic backscatter lidar measurements are essential for improving the accuracy of knowledge about cloud optical properties, such as extinction-to-backscatter ratio, from current space-based lidar systems. The extinction-to-backscatter ratio, also known as the lidar ratio, is defined for atmospheric scatterers as the ratio of the volume extinction coefficient (km^{-1}) to the volume backscatter coefficient ($km^{-1}\,sr^{-1}$), and typically varies from about 10 to 60 sr for tropospheric clouds (Del Guasta 2001; Whiteman et al. 2004). Perhaps most importantly, it is also an intermediate variable solved through iterations of the singular lidar equation used for the retrieval of extinction and backscatter coefficients from elastic backscatter lidar data (Fernald

Corresponding author address: John E. Yorks, Code 613.1, NASA Goddard Space Flight Center, Greenbelt, MD 20771.
E-mail: john.e.yorks@nasa.gov

DOI: 10.1175/2011JTECHA1507.1

© 2011 American Meteorological Society

Unauthenticated | Downloaded 04/29/24 02:28 PM UTC

et al. 1972). The CALIPSO Cloud–Aerosol Lidar with Orthogonal Polarization (CALIOP) and GLAS standard data products and processing algorithms apply a parameterized layer-specific lidar ratio to retrieve optical depth (Palm et al. 2002; Young et al. 2008; Young and Vaughan 2009). Therefore, the algorithms for these space-based lidars rely on an accurate global parameterization of the lidar ratio in order to resolve extinction and backscatter coefficients for ice and liquid water clouds (Winker et al. 2009b). A space-based lidar system that directly measures the lidar ratio is a favorable system for acquiring such statistics, but such a system will not exist until the launch of Earth Clouds, Aerosols, and Radiation Explorer (EarthCARE; Harris and Battrick 2001) scheduled for 2015. Currently, this parameterization can be constructed using ground-based and aircraft measurements, because the relatively large footprint size of current space-based elastic backscatter lidars, in combination with orbital heights in excess of 700 km, can produce a lower signal-to-noise ratio (SNR) and more significant multiple scattering effects than their ground-based and airborne counterparts at similar spatial scales (Vaughan et al. 2009). Recent studies have examined cirrus cloud optical properties using high spectral resolution lidars (Eloranta et al. 2001), Raman lidars (Reichardt et al. 2002a; Sakai et al. 2003; Whiteman et al. 2004), and elastic backscatter lidars (Platt et al. 1998; Sassen and Benson 2001; Del Guasta 2001; Platt et al. 2002).

Another significant parameter in the derivation of cloud properties from elastic backscatter lidar measurements is the depolarization ratio. The three primary types of linear depolarization ratios (LDRs) computed using backscatter data from atmospheric lidar systems with a linearly polarized laser are particulate depolarization ratio (PDR), molecular depolarization ratio (MDR), and volume depolarization ratio (VDR). VDR is defined as the ratio of the perpendicular total (molecular plus particulate) backscatter to the parallel total backscatter. In other words, VDR is the linear depolarization ratio of all of the substances occupying the sample volume (Cairo et al. 1999). PDR is defined as the perpendicular particulate backscatter to the parallel particulate backscatter, while MDR is defined as the perpendicular molecular backscatter to the parallel molecular backscatter. The LDR can be interpreted to better characterize particle morphology and cloud phase (Mishchenko and Hovenier 1995; Reichardt et al. 2002a). For liquid water clouds (spherical water particles) in the absence of multiple scattering, the LDR is near zero (Schotland et al. 1971). For nonspherical particles, such as ice crystals, significant amounts of depolarization (with values between 0.2 and 0.6) are observed (Sassen 1991). Both depolarization ratio and lidar ratio may vary as a function of temperature, geographic location, and/or cloud generation mechanism (Sassen and Benson 2001; Sassen and Comstock 2001; Reichardt et al. 2002a; Whiteman et al. 2004). Correlations between direct and simultaneous measurements of cirrus optical properties (i.e., lidar ratio and depolarization ratio) and particle microphysical properties have also been evaluated (Reichardt et al. 2002b; Wang and Sassen 2002; Sassen et al. 2003).

Lidar measurements of cirrus clouds obtained at visible wavelengths by Eloranta et al. (2001) as well as Sassen and Benson (2001) yielded a larger lidar ratio and smaller LDR values when compared to the ultraviolet cirrus measurements of Reichardt et al. (2002a). Despite differences in measurement wavelength, a wavelength effect is not the likely cause of this disagreement, unless there is a presence of significant concentrations of very small ice crystals in the cirrus clouds (Reichardt et al. 2002a). Whiteman et al. (2004) and Platt et al. (2002) also report conflicting lidar ratio values and trends when compared to previous studies. As noted in Reichardt et al. (2002a), the discrepancies in reported cirrus optical properties are probably due to differences in geographic locations at which the cirrus clouds were observed. Thus, the differences may be attributed to the varying atmospheric processes that are responsible for the cloud formation. These studies report important statistics of optical properties, which have been used as parameterizations in current space-based lidar systems. However, directly comparing the results of these above-mentioned studies to examine the link between lidar ratio and geographic location or meteorological season is complicated by differing lidar ratio retrieval techniques and corrections for multiple scattering effects between projects. Therefore, it is necessary to investigate the trends in these optical properties with geographic location or meteorological season using a dataset that reduces the above-mentioned inconsistencies. In this study, we examine airborne lidar data from the Cloud Physics Lidar (CPL; McGill et al. 2002) to determine correlations between lidar ratio and VDR, quantify trends in lidar ratio and VDR as a function of temperature and geographic location, and compare lidar ratio and VDR statistics with previous results.

2. Cloud physics lidar data and processing techniques

The CPL is an elastic backscatter lidar system operating at three wavelengths: 1064, 532, and 355 nm. VDR is determined by using the 1064 channel, and cloud optical properties are obtained using the backscattered signal at all 3 channels. The vertical resolution of the

Unauthenticated | Downloaded 04/29/24 02:28 PM UTC

CPL measurements is fixed at 30 m (McGill et al. 2002). For all data used in this study, CPL was mounted aboard the National Aeronautics and Space Administration (NASA) Earth Resources (ER)-2 aircraft. The nominal flight altitude of the ER-2 is ~20 km, which allows CPL to measure the full extent of the troposphere. CPL does not point at true nadir because the ER-2 nominally flies nose up at 2°, and the motion of the aircraft wings can cause changes in the pointing angle by an additional 1° during flight. Consequently, the contribution of specular reflection from horizontally oriented ice crystals should not influence CPL data products. Furthermore, CPL achieves full overlap at about 3–4 km below the aircraft. A near-pristine atmospheric zone, known as the calibration zone, is chosen between this height and the top of any cirrus measured (typically between 13 and 16 km for CPL) to match the lidar-attenuated backscatter signal to the attenuated Rayleigh profile and compute an accurate calibration coefficient (McGill et al. 2007).

There are many benefits to using the airborne CPL data for a study of cirrus lidar ratio and VDR. First, CPL has a higher SNR and a better transmittance measurement compared to a similar ground-based lidar system for high cirrus clouds as a consequence of a smaller range to target and the fact that the molecular backscatter increases with range for the CPL. Furthermore, ground-based lidar beams experience more attenuation as a consequence of aerosols and low-level clouds than the airborne CPL lidar beam through the thin molecular atmosphere. Also, the CPL has a footprint size of 2 m at the earth's surface (McGill et al. 2002), which is much smaller than that of satellite-based lidars and mitigates the impacts of multiple scattering effects compared to an instrument such as CALIOP, with a footprint size of 88 m at the earth's surface, as a result of being located about 700 km from scattering targets (Winker et al. 2009b). Since 2000, the CPL has flown on the high-altitude NASA ER-2 aircraft to retrieve high-resolution profiles of cloud properties from an altitude of about 20 km for over a dozen field campaigns, providing a reasonable dataset to study optical properties such as lidar ratio and VDR.

CPL data from five projects between 2003 and 2007 were analyzed at the 532- and 1064-nm wavelengths. The most recent study, the Tropical Composition, Cloud and Climate Coupling mission (TC4; Toon et al. 2010), was conducted in July–August 2007 and based in San Jose, Costa Rica (9.99°N, 84.21°W), with the primary goal of investigating cloud structure, properties, and processes in the tropical eastern Pacific. The Cloud and Land Surface Interaction Campaign (CLASIC; Miller 2008), a project with the purpose of studying the interaction of land processes and cumulus convection, was stationed in Houston, Texas (29.60°N, 95.16°W), during June 2007. A summer earlier, flights in July and August 2006 were performed from Warner-Robbins, Georgia (32.64°N, 83.59°W), as part of the CALIPSO-*CloudSat* Validation Experiment (CCVEX; McGill et al. 2007) and were intended to validate the newly launched CALIPSO and *CloudSat* satellites. Finally, data from the 2003 project The Observing System Research and Predictability Experiment (THORPEX; Shapiro and Thorpe 2004) was also examined. The first part of THORPEX, THORPEX-Pacific, was conducted from February to March 2003 in Honolulu, Hawaii (21.32°N, 157.92°W), while the second phase of the project, THORPEX-Atlantic, was held during November–December 2003 in Bangor, Maine (44.82°N, 68.83°W). The THORPEX campaigns supported the World Weather Research Program, with a goal of improving both short- and long-term weather forecasting. These five projects were chosen for this study to provide a range of meteorological seasons and geographic locations throughout North and Central America, as illustrated in Fig. 1, allowing for an evaluation of the relationship between cloud optical properties and geographic location, as well as meteorological season.

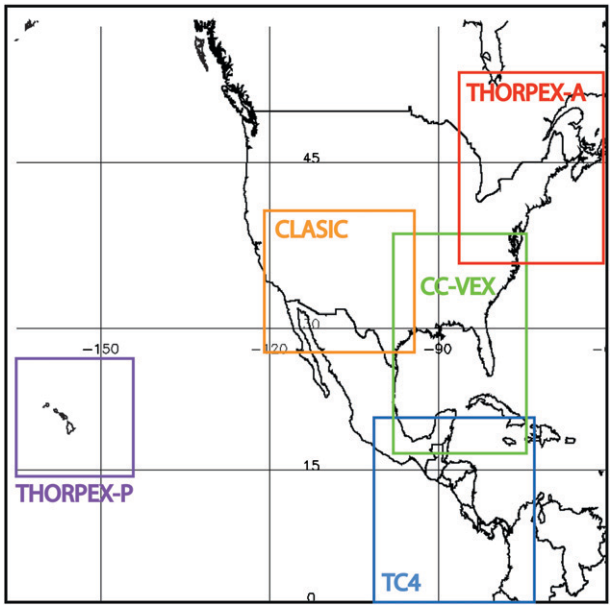

FIG. 1. A map of the continental United States and Hawaii displaying the approximate geographic locations in which cloud layers were detected for all five projects analyzed.

The same methods for determining the cloud layers and calculating the lidar ratio and VDR are used for all five projects analyzed in this study. Cloud layers are detected using the standard CPL processing algorithms. For each lidar backscatter profile, a threshold profile

Unauthenticated | Downloaded 04/29/24 02:28 PM UTC

is computed as the sum of the minimum attenuated backscatter coefficient and a constant fraction (modeled using CPL data) of the square root of the variance of the attenuated backscatter coefficient, as described by Palm et al. (2002). If the attenuated backscatter coefficient is above this threshold for three consecutive range bins, then these bins are designated a layer. The top height of the layer is located at the height where the highest of the consecutive samples is found and the bottom height of the layer is the height of the bin just above where the first of three consecutive below-threshold samples is located.

The lidar ratios reported in this study are layer-integrated values that are included in the standard CPL data products. The molecular transmission [$T_m^{2\sec\theta}(z)$], molecular backscatter coefficient [$\beta_m(z)$], and atmospheric temperature profiles were obtained using the World Meteorological Organization (WMO) upper-air station radiosonde that is closest in space and time to the ER-2 flight track for each flight. Luers and Eskridge (1998) report the uncertainties in the temperature profiles from these radiosonde instruments. The layer-integrated values of lidar ratio are determined by using a similar method to that of Fernald et al. (1972) and Spinhirne et al. (1980) by calculating an iterative best-fit lidar ratio based on measuring the cloud layer two-way transmittance loss as indicated by the reduction in CPL-measured molecular scattering below the transparent or semitransparent cloud bottom. The first step is to obtain values of effective particulate transmission squared, which by definition does not include a multiple scattering correction factor. The effective particulate transmission squared for a slant angle θ is defined as $T_p'^{2\sec\theta}(z_t)$ and $T_p'^{2\sec\theta}(z_b)$ at the top and bottom of the layer, respectively, where θ is the tilt angle of the instrument. The $T_p'^{2\sec\theta}(z_t)$ term is assumed to equal the $T_p'^{2\sec\theta}(z_b)$ term of all layers above the current layer, or 1.0 if there is no layer above. The $T_p'^{2\sec\theta}(z_b)$ term for the current layer can be estimated if the presumed clear atmosphere directly below the particulate layer is at least 616 m in physical thickness (i.e., 20 range bins) with a zone-mean (vertical average of all bins within the ''clear air'' zone) SNR greater than the 0.2 threshold for 532 nm (0.25 for 1064 nm). If the particulate layer meets these criteria, then the effective transmission $T_p'^{2\sec\theta}(z_b)$ is approximated by comparing the integrated lidar signal, which has been attenuated by the particulate layer in the presumed clear atmosphere (with a maximum thickness of 3 km) directly below the particulate layer (Γ_i), to the modeled integrated molecular signal, which is at the same altitude assuming that there is no attenuation by the cloud layer (Γ_0), as shown in the equation below from Spinhirne et al. (1996):

$$T_p'^{2\sec\theta}(z_b) = \frac{\Gamma_i}{\Gamma_0}. \tag{2.1}$$

This equation can also be written using the total attenuated backscatter coefficient at each height bin [$\beta'(z)$], the molecular backscatter assuming no attenuation by the cloud layer [$\beta_m(z)$], the molecular transmission calculated from the plane altitude to height z assuming no attenuation by the cloud layer [$T_m^{2\sec\theta}(z)$], the distance to the bottom of the particulate layer (z_b), and the distance to the end of the clear-air analysis zone (z_c),

$$T_p'^{2\sec\theta}(z_b) = \frac{\int_{z_b}^{z_c} \beta'(z)\, dz}{\int_{z_b}^{z_c} \beta_m(z) T_m^{2\sec\theta}(z)\, dz}. \tag{2.2}$$

This method is called the signal loss technique. The divisor incorporates the accumulated molecular transmission loss starting from the instrument height, assuming no cloud layer was detected.

The optical depth and the signal loss can then be quantified by the $T_p'^{2\sec\theta}(z_b)$ parameter. The equation for the cloud layer optical depth (τ_{layer}) is

$$\tau_{\text{layer}} = -0.50 \ln \frac{T_p'^{2\sec\theta}(z_b)}{T_p'^{2\sec\theta}(z_t)}. \tag{2.3}$$

To obtain the effective lidar ratio (S_p'), the transmission form of the slant angle lidar equation integrated over the layer from z_t to z_b is invoked. The equation is derived by Spinhirne et al. (1980), where $T_p'^{2\sec\theta}(z_b)$ is computed using Eq. (2.2) for an equally qualifying z_c and z_t,

$$T_p'^{2\sec\theta}(z_b) T_m^{2X\sec\theta}(z_b) = T_p'^{2\sec\theta}(z_t) T_m^{2X\sec\theta}(z_t) - 2\sec\theta \times \int_{z_t}^{z_b} S_p' \beta'(z) T_m^{2(X-1)\sec\theta}(z)\, dz, \tag{2.4}$$

where $X \equiv S_p'/S_m$. To simplify the equation, we can define the transmittance boundary condition at the top of any layer [$I_B(z_t)$], and similarly the bottom of any layer, as

$$I_B(z_h) = T_p'^{2\sec\theta}(z_h) T_m^{2X\sec\theta}(z_h). \tag{2.5}$$

If the particulate layer is the first layer that is encountered, then the term $T_p'^{2\sec\theta}(z_b)$ can be estimated as 1.00. The effective lidar ratio (S_p') can then be calculated through an iterative solution from the equation

$$S_p' = \frac{I_B(z_t) - I_B(z_b)}{2\sec\theta \int_{z_t}^{z_b} \beta'(z) T_m^{2(X-1)\sec\theta}(z)\, dz}, \tag{2.6}$$

Unauthenticated | Downloaded 04/29/24 02:28 PM UTC

assuming S'_p is constant through the particulate layer. The iterative process is started with an initial guess of S'_p as it relates to the X parameter, with the next iteration using the calculated value until the solution converges to a set tolerance of 0.08 sr. To convert the effective lidar ratio to the true lidar ratio (S_p), S'_p is divided by the multiple scattering factor (η) associated with the layer. For CPL, η is assumed to be 1.0 because multiple scattering effects are negligible for cirrus cloud measurements (McGill et al. 2003).

Uncertainties in the computed lidar ratio are a consequence of numerous issues. For example, the signal loss technique can induce uncertainties in the retrievals of lidar ratio for liquid water clouds when aerosols were present underneath the clouds. If we simplify Eq. (2.6) into two terms, the difference in the transmittance boundary condition (dI_B) and ξ as

$$dI_B = I_B(z_t) - I_B(z_b) \tag{2.7}$$

$$\xi = \sec\theta \int_{z_t}^{z_b} \beta'(z) T_m^{2(X-1)\sec\theta}(z)\, dz, \tag{2.8}$$

then the equation for the lidar ratio can be rewritten as

$$S'_p = \frac{dI_B}{2\xi}, \tag{2.9}$$

and the relative error in the lidar ratio retrieval can be estimated using the following equation:

$$\frac{\mathrm{VAR}(S'_p)}{S'^2_p} = \frac{\mathrm{VAR}(dI_B)}{dI_B^2} + \frac{\mathrm{VAR}(\xi)}{\xi^2}. \tag{2.10}$$

These two relative error terms can ultimately be traced back to three main sources of error in the lidar ratio retrievals. First and most important, clouds with weakly integrated attenuated backscatter, and therefore weak signal-to-noise ratios, increase the uncertainty in the lidar ratio calculation through the second term [from the relationship in Eq. (2.8)]. Thus, cloud layers with optical depths less than 0.1 were removed from the study. Second, the molecular transmission is also a source of error [from the dI_B term in Eqs. (2.5) and (2.7)].

The final main source of error in the lidar ratio estimates is due to uncertainties in the determination of the calibration constant, which were estimated to be less than 7% for the projects studied. The calibration constant (C) is determined by assuming that the precalibrated normalized relative backscatter coefficient (β_{nr}) divided by C should be equal to the attenuated molecular backscatter in the calibration zone; C can be introduced to Eq. (2.10) by substituting $\beta_{\mathrm{nr}}(z)/C$ for $\beta'(z)$ in Eq. (2.8). Precalibrated normalized relative backscatter is defined as the backscattered signal that has been corrected for range, dead time, overlap, and solar background. The equation for the determination of the calibration constant in the calibration zone is

$$C = \frac{\int_{z_t}^{z_b} \beta_{\mathrm{nr}}(z)\, dz}{\int_{z_t}^{z_b} \beta_m(z) T_m^{2\sec\theta}(z)\, dz}. \tag{2.11}$$

The uncertainties in the calibration constant likely arise from a combination of signal noise and the assumption of clear-air molecular scatter (Campbell et al. 2008; Vaughan et al. 2010). A multiple-scattering correction of lidar ratio was not necessary for the cloud layer cases discussed here because uncertainties in the lidar ratio caused by multiple scattering are much less than uncertainties resulting from the natural signal noise. Overall, conservative estimates of error values for cirrus cloud lidar ratios at 532 nm using CPL are about 10%, based solely on measurement statistics. Cloud layers with a lidar ratio or VDR that were three standard deviations greater than the mean, 58.2 sr and 0.69, respectively, were removed from the dataset, as well as opaque cloud layers with an optical depth greater than 2.8.

The linear layer-integrated VDR was calculated separately from the standard CPL data products using the ratio of the perpendicular polarized 1064-nm layer-integrated total attenuated backscatter coefficient (γ') to the parallel polarized 1064-nm layer-integrated total attenuated backscatter coefficient with the equation

$$\delta_{\mathrm{layer}} = \frac{\sum_{\mathrm{top}}^{\mathrm{base}} \gamma'_{1064\perp}(z)}{\sum_{\mathrm{top}}^{\mathrm{base}} \gamma'_{1064\parallel}(z)}. \tag{2.12}$$

This computation was performed for each transparent cloud layer detected in the CPL data in which the lidar ratio was calculated using the signal loss technique, with a horizontal resolution of 200 m. The main source of error is the determination of the relative calibration for the individual 1064-nm detectors, known as the depolarization gain ratio (Liu et al. 2004; Hu et al. 2006). Errors in the depolarization gain ratio for CPL were determined to be less than 3% for the THORPEX-Pacific cases (Liu et al. 2004). Another source of error in the VDR derived from CPL is the 3% cross talk measured in the CPL receiver subsystem. Despite the small FOV of the CPL instrument, multiple scattering can also lead to

Unauthenticated | Downloaded 04/29/24 02:28 PM UTC

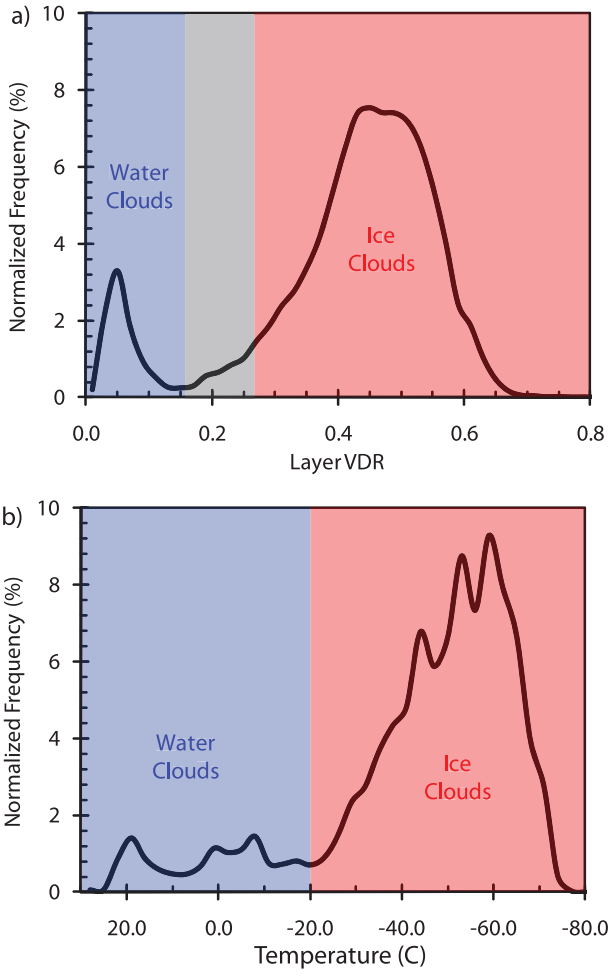

FIG. 2. A frequency distribution of (a) VDR and (b) temperature for all cloud layers with a lidar ratio calculated using the signal loss technique detected by CPL from 2003 to 2007 normalized to the total number of cloud layers analyzed (83 610). The shaded areas represent the clouds layers defined as liquid water clouds (blue) and ice clouds (red). The gray shaded area in (a) represents cloud layers in which the phase cannot be accurately characterized.

a small bias in VDR for liquid water clouds. Hu et al. (2006) demonstrated a relationship between the accumulated single scattering fraction and accumulated depolarization ratio for liquid water clouds with a wide range of extinction coefficients, mean droplet sizes, and lidar FOV. These multiple scatter effects are more problematic for liquid water clouds retrievals than ice cloud retrievals because the values of VDR are much smaller for liquid water clouds.

The distribution of the layer-integrated VDRs for all cloud layers detected by CPL in which the lidar ratio is calculated using the signal loss technique is shown in Fig. 2a (normalized to the 83 610 total profiles in which the lidar ratio was calculated for a cloud layer). Two distinct peaks are observed in the data. The first, at roughly 0.05, represents liquid water clouds and ranges from 0.0 to about 0.09. These values are slightly larger than those determined by Schotland et al. (1971) for liquid water clouds, which are attributed to the cross talk from the previously described CPL receiver. The second peak at 0.45 signifies ice clouds, consistent with the values computed by Sassen and Benson (2001), Platt et al. (2002), and Reichardt et al. (2002a). The distribution of the midcloud temperatures for all cloud layers detected by CPL in which the lidar ratio is calculated using the signal loss technique is shown in Fig. 2b. This distribution increases at temperatures below −20° and peaks at −60°C, representing the ice cloud population. In this study, the VDR and midcloud temperature distributions are used to discriminate cloud phase when analyzing the lidar ratio trends. Clouds with a VDR less than 0.16, midcloud temperature warmer than −20°C, and midcloud altitude less than 8 km are considered liquid water clouds. Ice clouds are defined as clouds with a VDR greater than 0.27, a midcloud temperature of less than −20°C, and a midcloud altitude of greater than 8 km. These VDR thresholds for cloud discrimination are consistent with the results of Hu et al. (2009) for liquid water clouds and randomly oriented ice clouds, and Sassen and Benson (2001) for cirrus clouds. Furthermore, 96% of the zenith measurements of cirrus clouds from Sassen and Benson (2001) correspond with temperatures below −20°C. The residual clouds, with VDRs between 0.16 and 0.27, are considered to be complex cloud phases that cannot be accurately resolved and are therefore not included in this study. These thresholds partition the lidar ratio observations into two cloud phase datasets for analysis.

3. Observations of cloud optical properties

a. Lidar ratio distributions and statistics

Over 80 000 cloud layers were observed by CPL between 2003 and 2007 in which the lidar ratio is directly calculated using the transmission loss method. Descriptive statistics, such as mean, median, standard deviation, and relative error (defined as the standard deviation divided by the mean), for lidar ratio, VDR, and cloud optical depth (COD) are reported for all five projects and all of the CPL data analyzed for ice clouds in Table 1. It should be noted that the relative error includes contributions from the retrieval uncertainties explained in section 2, as well as the natural variability of the clouds sampled. Lidar ratio frequency distributions for ice clouds are plotted in Fig. 3 for all five projects examined in this study. For ice clouds, the lowest lidar ratios are observed during THORPEX-Atlantic, with

Unauthenticated | Downloaded 04/29/24 02:28 PM UTC

TABLE 1. Statistics for ice clouds from CPL for projects listed.

	CCVEX	CLASIC	TC4	THORPEX-A	THORPEX-P	All data
Samples	15 828	12 390	27 293	9533	8469	73 513
Mean S (sr)	30.68	30.62	26.18	21.65	25.38	27.23
Median S (sr)	28.53	28.97	24.57	20.80	24.06	25.24
Std dev S (sr)	10.79	11.70	9.67	7.82	9.84	10.56
Error* S (%)	35.16	38.21	36.93	36.11	38.78	38.77
Mean δp	0.509	0.400	0.424	0.496	0.401	0.445
Median δp	0.516	0.403	0.424	0.509	0.384	0.444
Std dev δp	0.071	0.064	0.063	0.068	0.092	0.083
Error* δp (%)	14.00	16.02	14.90	13.74	23.02	18.57
Mean COD	0.397	0.316	0.334	0.453	0.443	0.373
Median COD	0.337	0.255	0.264	0.404	0.367	0.301
Std dev COD	0.249	0.201	0.230	0.259	0.279	0.245
Error* COD (%)	62.81	63.49	68.77	57.29	63.02	65.76

* Includes natural variability and instrument retrieval uncertainty.

a median of 20.80 ± 7.82 sr and a peak in the lidar ratio frequency at 23.0 sr. The peak (or mode) lidar ratio for TC4 and CCVEX is 27 sr, with median values of 24.57 ± 9.67 and 28.53 ± 10.79 sr, respectively. Also of note, ice cloud lidar ratios above 40.0 sr are detected more frequently during CLASIC than any other projects, causing the highest median value of any project (28.97 ± 11.70). Finally, lidar ratio frequency distributions for ice clouds are plotted in Fig. 3e for all CPL data from 2003 to 2007. The peak of the ice cloud distribution is 25.0 sr, which is very close to the median values of 25.24 ± 10.56 sr. This value for ice clouds is in agreement with the CALIOP algorithm, which assumes a lidar ratio of 25.0 sr for ice clouds when the ratio cannot be computed because of particulate contamination below the layer (Winker et al. 2009b). Overall, the majority (84%) of the ice cloud layers yield a lidar ratio between 10.0 and 40.0 sr, which compares favorably with the lidar ratio distributions for the ice cloud observations of Eloranta et al. (2001) and Reichardt et al. (2002b).

For liquid water clouds a much smaller sample size was observed for each of the five projects, so only overall statistics are presented. Figure 4 shows the cloud mid-height frequency, normalized by the number of clouds observed for the particular project and plotted with increasing altitude. The liquid water clouds observed in which lidar ratios are computed using the signal loss technique are primarily physically thin and broken boundary layer cumulus clouds between 1 and 3 km and physically thin and broken altocumulus clouds between 4 and 8 km. Figure 5 displays liquid water cloud lidar ratio frequencies for all of the CPL data analyzed, with subsets for clouds above and below 4 km. Liquid water clouds above 4 km, which are primarily physically thin and broken altocumulus clouds, have a very different distribution in lidar ratio, with a peak near about 16.0 sr, compared to liquid water clouds below 4 km, which have a peak near 11.0 sr. The lower lidar ratios for clouds below 4 km were likely a consequence of the presence of aerosols below the cumulus layer. To compute the lidar ratio using the transmission loss method, one must assume that only Rayleigh scattering occurs below the cloud layer. This assumption is invalid in the presence of aerosols, and thus aerosols near the earth's surface cause an overestimation of the two-way transmittance and in turn decrease the lidar ratio. Therefore, lidar ratio statistics are only reported for altocumulus clouds in this study. Overall, the mean and median values of lidar ratio for these altocumulus clouds between 4 and 8 km were 20.41 ± 10.91 and 17.29 ± 10.91 sr (Table 2), respectively, and were nearly identical to liquid water cloud lidar ratios found in previous studies (O'Connor et al. 2004; Hu et al. 2007).

b. *Ice clouds optical properties*

In this section we examine the relationship between ice cloud lidar ratio and VDR, as well as the correlation of these optical parameters with temperature and geographic locations. To explore the correlations between lidar ratio and temperature, the median lidar ratio is calculated for temperature bins of 3°C, for all five projects, and plotted in Fig. 6. The bars shown in Fig. 6 represent one standard deviation of the sample values in each bin. Values of lidar ratio range from 10.0 ± 3.0 to 35.0 ± 12.0 sr, with CCVEX and CLASIC reporting slightly higher values, greater than 30.0 ± 11.0 sr, than other locations. During the TC4, CLASIC, and THORPEX-Pacific projects, the median lidar ratio decreases with decreasing temperature between −40° and −60°C (THORPEX-Pacific more than others). The CLASIC data reveal anomalously high (50 ± 10 sr) lidar ratio values between −65° and −70°C. This is not

Unauthenticated | Downloaded 04/29/24 02:28 PM UTC

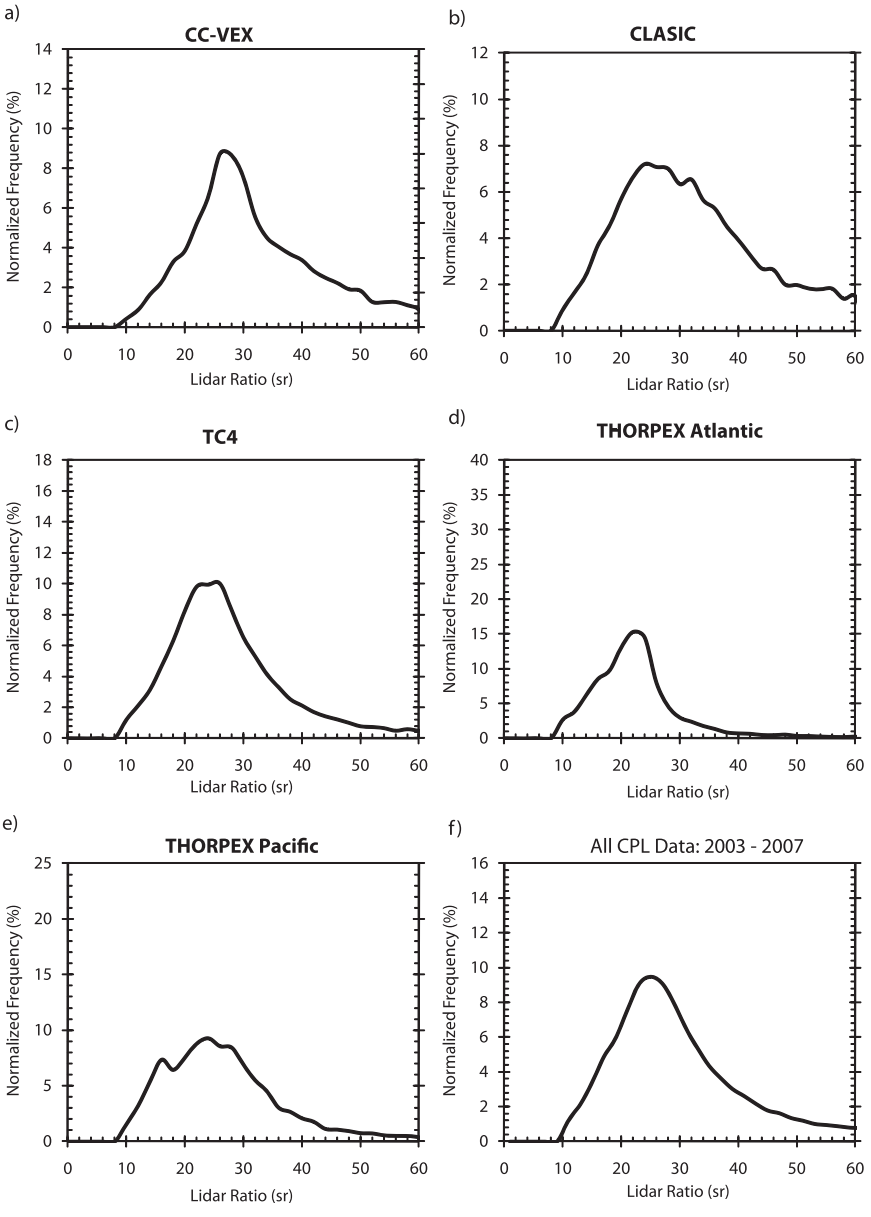

FIG. 3. The frequency distributions of lidar ratio (sr) for ice clouds for (a) CCVEX, (b) CLASIC, (c) TC4, (d) THORPEX-Atlantic, (e) THORPEX-Pacific, and (f) all CPL data from 2003 to 2007. Number of cloud layer samples reported in Table 1 are used to normalize each distribution.

statistically significant due to a lack of cloud layer samples in this region, because it is composed of less than 1% of the entire CLASIC ice cloud dataset. Also, anomalously low lidar ratios are observed during THORPEX-Pacific between −50° and −70°C. The possible origin of these low values for THORPEX-Pacific will be discussed later in the section. On average, lidar ratio appears to be decreasing slightly with decreasing temperature (Fig. 6f). However, this trend is not statistically significant, because the lidar ratio only decreases 3–5 sr and the uncertainty in the dataset is larger.

The relationship between lidar ratio and VDR is investigated by computing the median lidar ratio for VDR bins of 0.02. The results for all five projects, as well as the mean of all five projects, are shown in Fig. 7. Lidar ratio values range from roughly 14.0 ± 3.0 to 45.0 ± 12.0 sr. Lidar ratios measured in CLASIC and CCVEX are near constant at about 30.0 ± 10.0 sr as VDR increases from

Unauthenticated | Downloaded 04/29/24 02:28 PM UTC

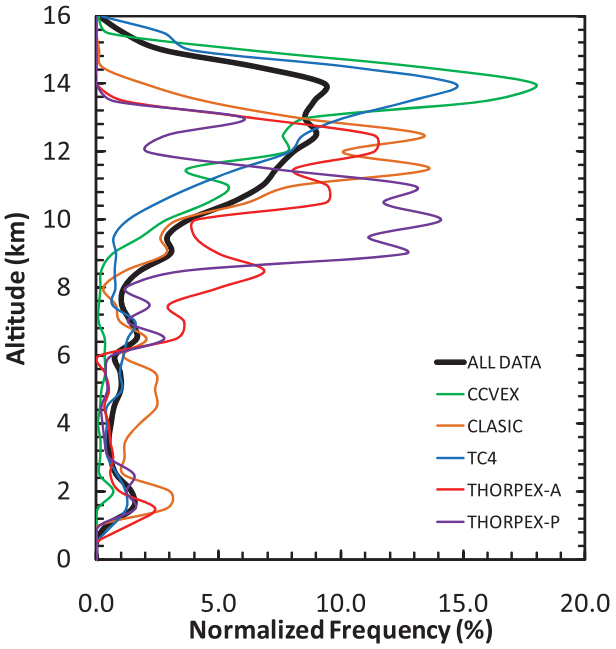

FIG. 4. The frequency distributions of altitude (midheight, km) for all clouds for CCVEX, CLASIC, TC4, THORPEX-Atlantic, THORPEX-Pacific, and all CPL data from 2003 to 2007 normalized to the number of cloud layers sampled in each respective project.

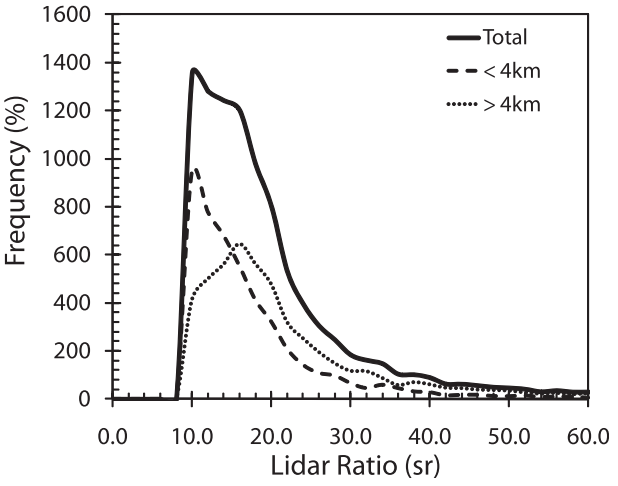

FIG. 5. The frequency distributions of lidar ratio for liquid water clouds for all CPL data from 2003 to 2007, with subsets of data for clouds with a midheight greater than 4 km (dotted line) and clouds with a midheight higher than 4 km (dashed line).

0.30 to 0.50, while during THORPEX-Atlantic lidar ratios are consistently around 20.0 ± 7.0 sr for the same range, which is lower than the other locations. Additionally, lidar ratios detected during TC4 and THORPEX-Pacific decrease from about 27.0 ± 10.0 sr to 14.0 ± 3.0 sr with increasing VDR between 0.35 and 0.60. Reichardt et al. (2002a) also find a similar relationship between VDR and lidar ratio when VDR is high in the midlatitudes. However, data from CCVEX show the opposite trend, similar to the results of Hu (2007). Also, it should be noted that the deviation from the trend in the CLASIC data above 0.5 is not statistically significant as previously discussed (Fig. 7b).

The lidar ratio values and trends observed in Figs. 6 and 7 are quite different across projects. Lidar ratios measured during THORPEX-Atlantic remain low, roughly 20.0 ± 7.0 sr, compared to the other four projects (Fig. 6). Because this project is farthest north and was conducted during the fall–winter months of November and December, results are different for the other four projects in which ice particles formed in convective environments with rapid upward air motions. Measurements obtained during CLASIC and CCVEX depict higher lidar ratios than TC4 and THORPEX-Pacific. Furthermore, the median lidar ratio significantly decreases with both decreasing temperature and increasing VDR during the THORPEX-Pacific project, trends that are observed to be weaker for the other four projects. This could be attributed to the likely less polluted marine air masses sampled during THORPEX-Pacific project compared to the other projects. The trend of lidar ratio decreasing with decreasing temperature (Fig. 6e) is a trend previously detected by Whiteman et al. (2004) for hurricane ice clouds in the tropical Atlantic, Reichardt et al. (2002a) for cirrus in the arctic, and Chen et al. (2002) for cirrus clouds using a elastic backscatter lidar over Taiwan. However, other projects, such as Whiteman et al. (2004) for nonhurricane cases and Platt et al. (2002) for ice clouds in tropical Australia, find the opposite trend. These results demonstrate that

TABLE 2. Statistics for liquid water clouds from CPL data. N/A is not applicable.

	All data	Clouds, height > 4 km
Samples	10 097	5250
Mean S (sr)	N/A	20.41
Median S (sr)	N/A	17.29
Std dev S (sr)	N/A	10.91
Error* S (%)	N/A	53.46
Mean δp	0.045	0.037
Median δp	0.035	0.026
Std dev δp	0.034	0.034
Error* δp (%)	76.13	92.51
Mean COD	0.423	0.447
Median COD	0.321	0.335
Std dev COD	0.328	0.358
Error* COD (%)	77.55	80.09

* Includes natural variability and instrument retrieval uncertainty.

Unauthenticated | Downloaded 04/29/24 02:28 PM UTC

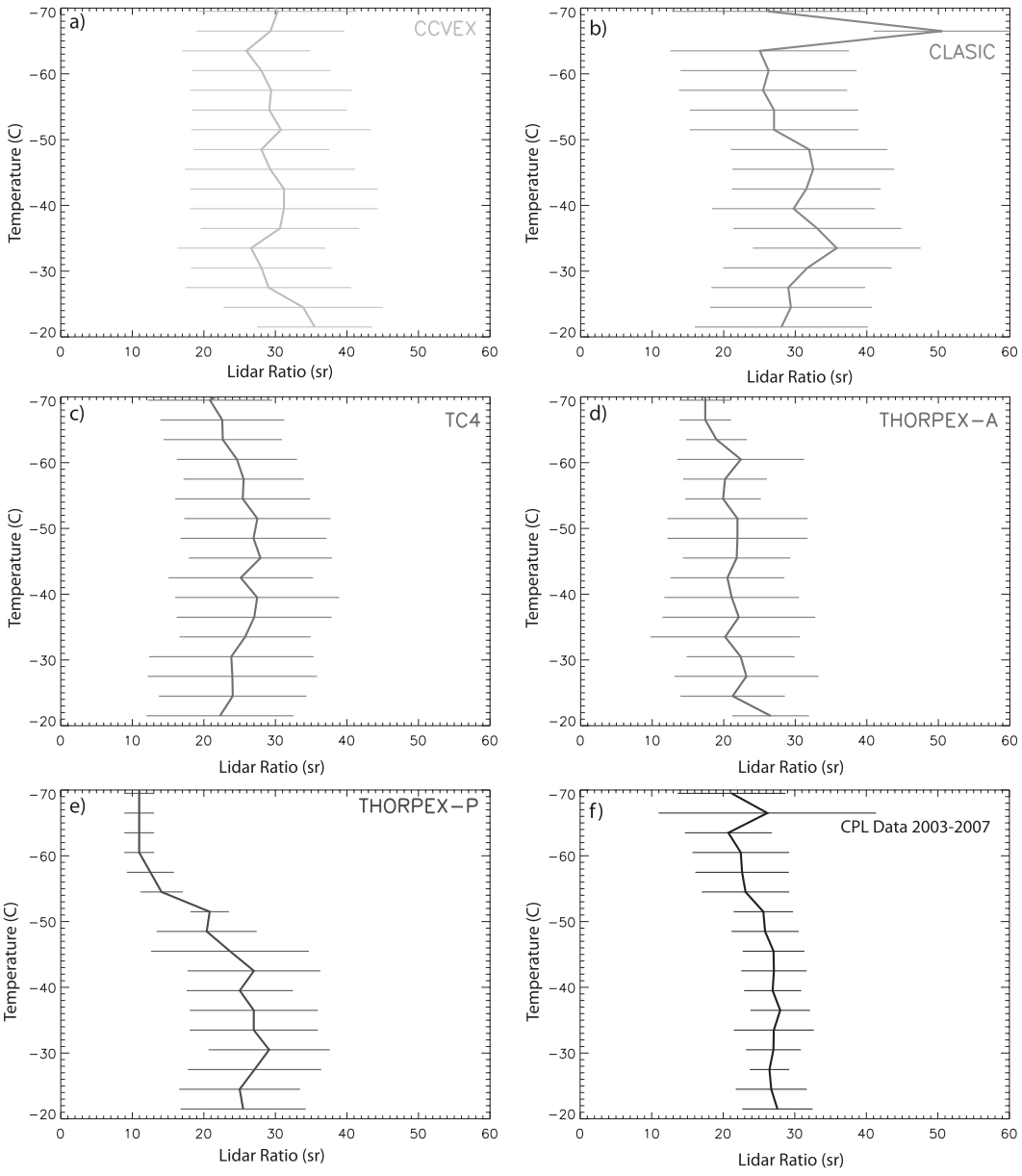

FIG. 6. Ice cloud lidar ratio (sr) values are plotted as a function of temperature (°C), using the median lidar ratio of temperature bins of 3°C for (a) CCVEX, (b) CLASIC, (c) TC4, (d) THORPEX-Atlantic, (e) THORPEX-Pacific, and (f) the mean of the five projects. The error bars represent ±1 standard deviation of the data contained in the respective bin.

differences in lidar ratio trends and values for cirrus clouds are found between CPL projects, and therefore are different for varying geographic locations and meteorological seasons.

Values and trends of VDR as a function of temperature are evaluated by retrieving the median VDR for temperature bins of 2°C, as demonstrated in Fig. 8. Values of VDR range from about 0.30 ± 0.06 to 0.59 ± 0.04. Also observed in CPL data is a trend of increasing VDR with decreasing temperatures, which is very consistent throughout all geographic locations and meteorological seasons. On average, the VDR increases roughly 0.15 from −20° to −70°C (Fig. 8f), consistent with the relationship determined by Sassen and Benson (2001), Platt et al. (2002), and Reichardt et al. (2002a). Perhaps the sharpest increase in VDR with decreasing temperature is detected during the THORPEX-Pacific project (Fig. 8e). During this project, VDRs are greater than

Unauthenticated | Downloaded 04/29/24 02:28 PM UTC

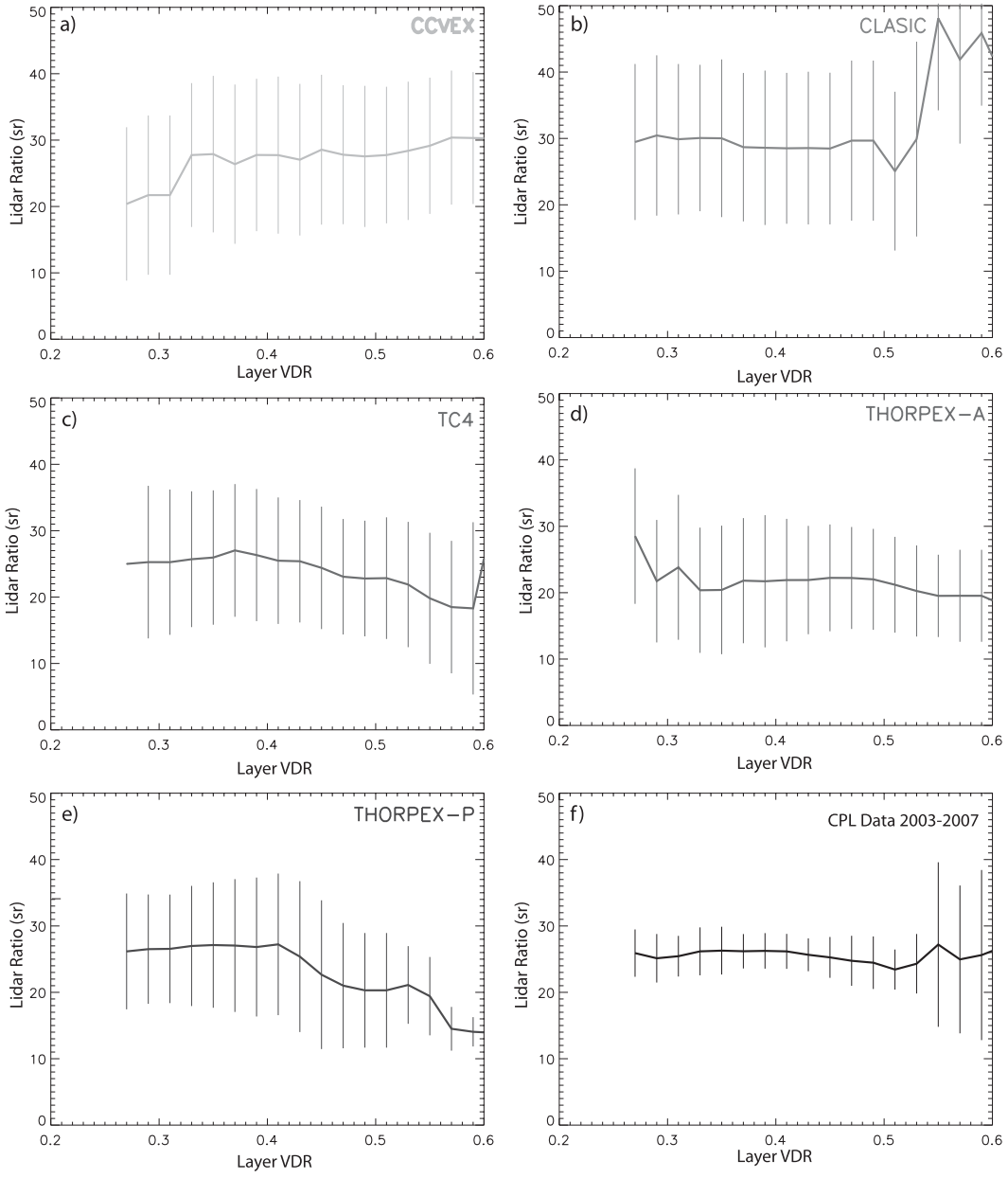

FIG. 7. As in Fig. 6, but plotted as a function of VDR using the median lidar ratio of VDR bins of 0.02.

0.50 ± 0.05 for temperatures less than −45°C, which is much higher than the other four projects and the mean for all CPL data (Table 1). Furthermore, cloud layers with high VDR during THORPEX-Pacific correspond to low values of the lidar ratio. The VDRs are similar to those collected during the Tropical Ocean and Global Atmosphere Coupled Ocean–Atmosphere Response Experiment (TOGA COARE; Webster and Lukas 1992) project for the same temperature range in the western Pacific. Sassen and Benson (2001) report LDRs obtained over the midlatitudes (Salt Lake City, Utah) that are lower than those obtained during TOGA COARE (Sassen et al. 2000). They suggest this could be attributed to the distinct relatively fresh and pristine cirrus particles observed during TOGA COARE, similar to the THORPEX-Pacific project.

c. Liquid water cloud optical properties

Several studies have investigated optical properties of liquid water clouds using lidar systems (Schotland et al. 1971; Pinnick et al. 1983; Del Guasta et al. 1993; Muller et al. 1998; O'Connor et al. 2004). In this section, we

Unauthenticated | Downloaded 04/29/24 02:28 PM UTC

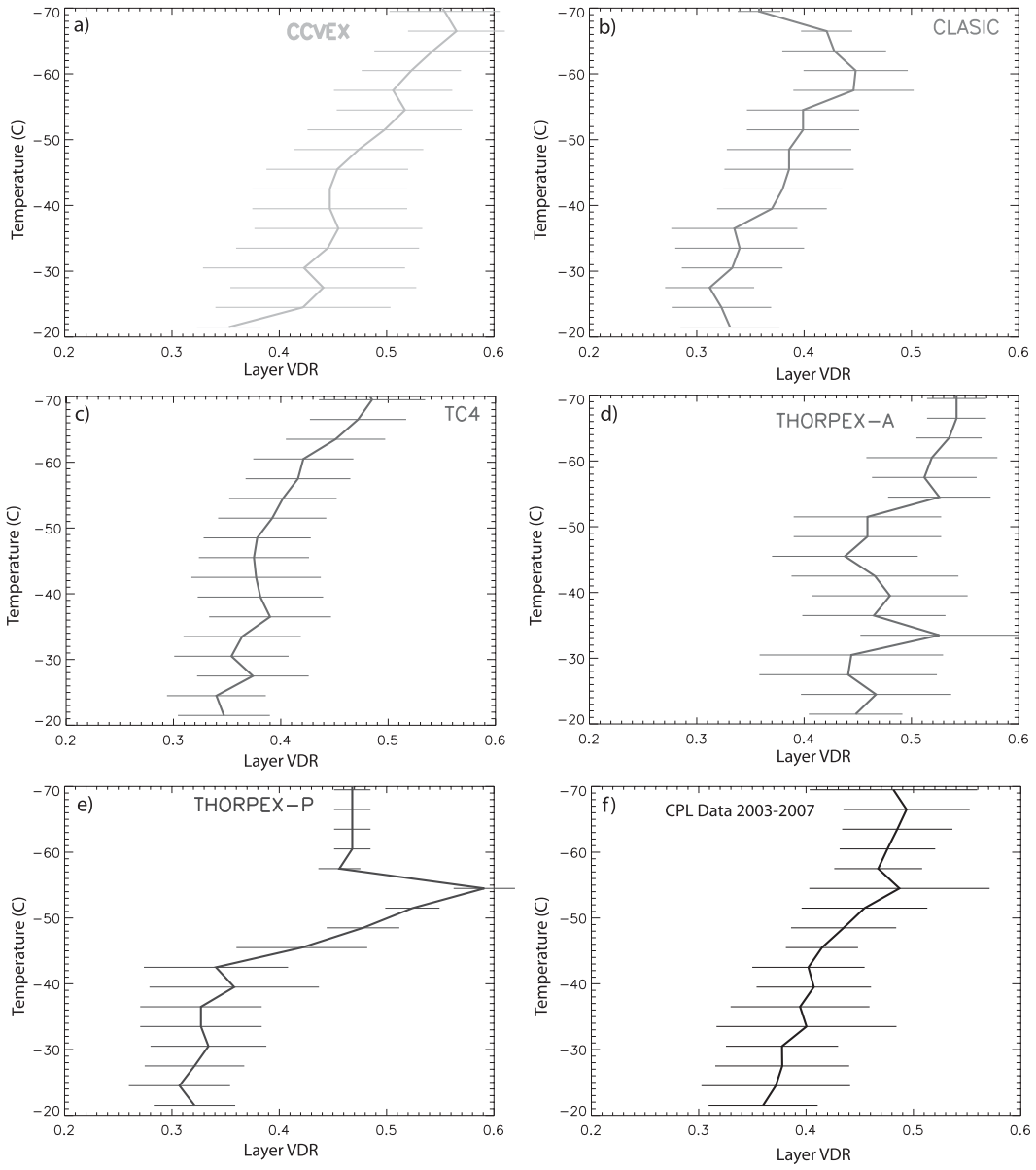

FIG. 8. As in Fig. 6, but plotted as a function of temperature (°C) using the median VDR of temperature bins of 3°C.

assess the relationship between VDR and temperature for liquid water clouds, as well as describe statistics of lidar ratio for altocumulus clouds. As previously discussed in section 3a, the inherent uncertainties in lidar ratio were larger for liquid water clouds below 4 km than for ice clouds or altocumulus clouds as consequence of aerosols near the earth's surface. Mean and median values of lidar ratio for altocumulus clouds between 4 and 8 km were 20.41 ± 10.91 and 17.29 ± 10.91 sr (Table 2), respectively, which compare favorably with the values of about 15.0 to 23.0 sr measured by Pinnick et al. (1983), Dubinsky et al. (1985), and Del Guasta et al. (1993). The relationship between VDR and temperature for all liquid water clouds analyzed (boundary layer cumulus and altocumulus) is illustrated in Fig. 9, with values of VDR ranging from 0.03 ± 0.02 to 0.07 ± 0.02. Overall, the mean and median VDR for all CPL data is 0.045 ± 0.034 and 0.035 ± 0.034, respectively (Table 2). Previously, Muller et al. (1998) found depolarization ratios of boundary layer clouds to be less than 0.03, while Del Guasta et al. (1993) found depolarization ratios of less than 0.1 frequently in clouds with temperatures greater than −20°C. No relationship between VDR and temperature is observed for liquid water clouds, which is

Unauthenticated | Downloaded 04/29/24 02:28 PM UTC

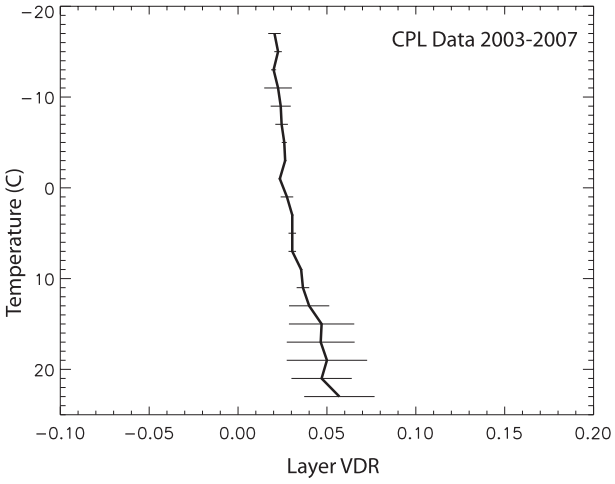

FIG. 9. Liquid water cloud VDR values are plotted as a function of temperature (°C), using the median VDR of temperature bins of 2°C for all liquid water clouds. The error bars represent ±1 standard deviation of the data contained in the respective bin.

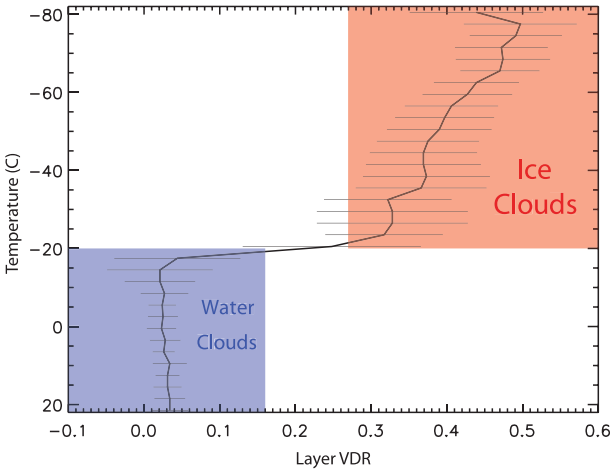

FIG. 10. VDR values are plotted as a function of temperature (°C), using the median VDR of temperature bins of 3°C for all cloud phases during TC4. The cloud layers defined as liquid water clouds (blue) and ice clouds (red) are represented. The error bars signify ±one standard deviation of the data contained in the respective bin.

expected because all liquid water particles are theorized to be ''perfect'' spheres. To put this lack of trend into context with the ice clouds, VDR is plotted as a function of temperature (°C) in Fig. 10, using the median VDR of temperature bins of 3°C for all cloud phases during TC4. Between temperatures of 20° and −15°C the VDR remains relatively constant at a value of nearly 0.03 ± 0.02 before increasing to 0.16 ± 0.07 at −20°C, dominated by water particles. The optically thin clouds measured by CPL tend to remain in liquid phase until −15° to −20°C in the tropics. For temperatures less than −20°C and VDRs greater than 0.27 ± 0.10, ice cloud observations dominate the curve. The VDR thresholds determined in this study are now standard in the CPL processing algorithms. The temperature thresholds from Fig. 10 are used in the event accurate VDR data cannot be computed for a layer.

4. Conclusions

In this paper describing the relationship between cloud optical properties and variables such as temperature and geographic location, we present an extended record of lidar ratios and VDRs using the CPL airborne elastic backscatter lidar. The cloud layer–integrated lidar ratios and VDRs from CPL provide a sufficient dataset to begin to quantify trends in cloud optical properties as a function of temperature and geographic location for a multitude of reasons. First, CPL has been included in over a dozen field campaigns in various geographic locations using the same detection wavelengths (532 and 1064 nm). Also, because CPL flies at an altitude of 20 km, the method of calculating lidar ratio using molecular backscatter at cloud bottom is advantageous for optically thin ice clouds. Finally, the CPL field of view (FOV) and footprint size are small enough that multiple scattering corrections are not needed for lidar ratio retrievals. Therefore, correlations between cloud optical properties and temperature are evaluated with a consistent method for computing lidar ratio over several geographic locations and meteorological seasons.

The analysis of all CPL data from 2003 to 2007 presented here indicates that the majority of the ice cloud layers yield a lidar ratio between 10.0 and 40.0 sr, with the lidar ratio frequency distribution centered at 25.0 sr for ice clouds and 16.0 sr for liquid water clouds above 4 km (altocumulus). There are no statistically significant trends in lidar ratio with temperature or VDR for ice clouds when analyzing the average over all five projects. However, when the data are separated into geographic regions, distinct trends are detected for specific locations. During THORPEX-Pacific, lidar ratio decreases with decreasing temperature, a trend that was previously detected by Whiteman et al. (2004), Reichardt et al. (2002a), and Chen et al. (2002) for cirrus clouds. Finally, when examining VDR and temperature, there is no relationship between the two parameters for liquid water clouds. However, for ice clouds, the VDR increases significantly as temperatures decreases. This dependence of depolarization ratio on temperature agrees with findings of Sassen and Benson (2001), Platt et al. (2002), and Reichardt et al. (2002a). The thresholds of cloud phase determined from statistics of cloud VDR and

Unauthenticated | Downloaded 04/29/24 02:28 PM UTC

temperature presented can be invoked in future lidar cloud phase discrimination algorithms. Observed trends and values of ice cloud optical properties vary by geographic location and meteorological season. In nonideal conditions, an accurate parameterization of the lidar ratio for ice and liquid water clouds is fundamental for current space-based lidar systems to accurately compute extinction and backscatter coefficients. This parameterization should account for the dependence of lidar ratio on geographic location. However, more research is needed to improve our understanding of the relationship between lidar ratio and cloud generation mechanism, which consequently should improve the accuracy of cloud radiative forcing estimations from space-based instruments.

Acknowledgments. The Cloud Physics Lidar is sponsored by NASA's Radiation Sciences Program.

REFERENCES

Cairo, F., G. Di Donfrancesco, A. Adriani, L. Pulvirenti, and F. Fierli, 1999: Comparisons of various linear depolarization parameters measured by lidar. *Appl. Opt.,* **38,** 4425–4432.

Campbell, J. R., K. Sassen, and E. J. Welton, 2008: Elevated cloud and aerosol layer retrievals from micropulse lidar signal profiles. *J. Atmos. Oceanic Technol.,* **25,** 685–700.

Chen, W. N., C. W. Chiang, and J. B. Nee, 2002: Lidar ratio and depolarization ratio for cirrus clouds. *Appl. Opt.,* **41,** 6470–6476.

Del Guasta, M., 2001: Simulation of LIDAR returns from pristine and deformed hexagonal ice prisms in cold cirrus clouds by means of ''face tracing.'' *J. Geophys. Res.,* **106,** 12 589–12 602.

——, M. Morandi, L. Stefanutti, J. Brechet, and J. Piquard, 1993: One year of cloud lidar data from Dumont d'Urville (Antarctica), 1, General overview of geometrical and optical properties. *J. Geophys. Res.,* **98,** 18 575–18 587.

Dubinsky, R. H., A. I. Carswell, and S. R. Pal, 1985: Determination of cloud microphysical properties by laser backscattering and extinction measurements. *Appl. Opt.,* **24,** 1614.

Eloranta, E. W., R. E. Kuehn, and R. E. Holz, 2001: Measurements of backscatter phase function and depolarization in cirrus clouds made with the University of Wisconsin High Spectral Resolution Lidar. *Advances in Laser Remote Sensing,* A. Dabas, C. Loth, and J. Pelon, Eds., Ecole Polytechnique Paris, 255–257.

Fernald, F. G., B. M. Herman, and J. A. Reagan, 1972: Determination of aerosol height distributions with lidar. *J. Appl. Meteor.,* **11,** 482–489.

Harris, R., and B. Battrick, 2001: EarthCARE—Earth Clouds, Aerosols and Radiation Explorer. ESA Rep. SP-1257 (1), 130 pp.

Hu, Y., 2007: Depolarization ratio–effective lidar ratio relation: Theoretical basis for space lidar cloud phase discrimination. *Geophys. Res. Lett.,* **34,** L11812, doi:10.1029/2007GL029584.

——, Z. Liu, D. Winker, M. Vaughan, V. Noel, L. Bissonnette, G. Roy, and M. McGill, 2006: A simple relation between lidar multiple scattering and depolarization for water clouds. *Opt. Lett.,* **31,** 1809–1811.

——, and Coauthors, 2007: The depolarization–attenuated backscatter relation: CALIPSO lidar measurements vs. theory. *Opt. Lett.,* **15,** 5327–5332.

——, and Coauthors, 2009: CALIPSO/CALIOP cloud phase discrimination algorithm. *J. Atmos. Oceanic Technol.,* **26,** 2293–2309.

Liu, Z., M. McGill, Y. Hu, C. A. Hostetler, M. Vaughan, and D. Winker, 2004: Validating lidar depolarization calibration using solar radiation scattered by ice clouds. *Geosci. Remote Sens. Lett.,* **1,** 157–161, doi:10.1109/LGRS.2004.829613.

Luers, J. K., and R. E. Eskridge, 1998: Use of radiosonde temperature data in climate studies. *J. Climate,* **11,** 1002–1019.

McGill, M. J., D. Hlavka, W. Hart, V. S. Scott, J. Spinhirne, and B. Schmid, 2002: Cloud physics lidar: Instrument description and initial measurement results. *Appl. Opt.,* **41,** 3725–3734.

——, ——, ——, E. J. Welton, and J. R. Campbell, 2003: Airborne lidar measurements of aerosol optical properties during SAFARI-2000. *J. Geophys. Res.,* **108,** 8493, doi:10.1029/2002DJ002370.

——, M. A. Vaughan, C. R. Trepte, W. D. Hart, D. L. Hlavka, D. M. Winker, and R. Kuehn, 2007: Airborne validation of spatial properties measured by the CALIPSO lidar. *J. Geophys. Res.,* **112,** D20201, doi:10.1029/2007JD008768.

Miller, M. A., 2008: The Cloud and Land Surface Interaction Campaign (CLASIC). *Eos, Trans. Amer. Geophys. Union,* **89** (23), Abstract H43D-03.

Mishchenko, M. I., and J. W. Hovenier, 1995: Depolarization of light backscattered by randomly oriented nonspherical particles. *Opt. Lett.,* **20,** 1356–1358.

Muller, D., U. Wandinger, D. Althausen, I. Mattis, and A. Ansmann, 1998: Retrieval of physical particle properties from lidar observations of extinction and backscatter at multiple wavelengths. *Appl. Opt.,* **37,** 2260–2263.

O'Connor, E. J., A. J. Illingworth, and R. J. Hogan, 2004: A technique for autocalibration of cloud lidar. *J. Atmos. Oceanic Technol.,* **21,** 777–786.

Palm, S. P., W. D. Hart, D. L. Hlavka, E. J. Ellsworth, A. Mahesh, J. D. Spinhirne, 2002: Geoscience Laser Altimeter System (GLAS) atmospheric data products. ICESat/GLAS Algorithm Theoretical Basis Document, 141 pp. [Available online at http://www.csr.utexas.edu/glas/pdf/glasatmos.atbdv4.2.pdf.]

Pinnick, R. G., S. G. Jennings, P. Chylek, C. Ham, and W. T. Grandy, 1983: Backscattering and extinction in water clouds. *J. Geophys. Res.,* **88** (C11), 6787–6796.

Platt, C. M. R., S. A. Young, P. J. Manson, G. R. Patterson, S. C. Marsden, R. T. Austin, and J. H. Churnside, 1998: The optical properties of equatorial cirrus from observations in the ARM Pilot Radiation Observation Experiment. *J. Atmos. Sci.,* **55,** 1977–1996.

——, ——, R. T. Austin, G. R. Patterson, D. L. Mitchell, and S. D. Miller, 2002: LIRAD observations of tropical cirrus clouds in MCTEX. Part I: Optical properties and detection of small particles in cold cirrus. *J. Atmos. Sci.,* **59,** 3145–3162.

Rajeevan, M., and J. Srinivasan, 2000: Net cloud radiative forcing at the top of the atmosphere in the Asian monsoon region. *J. Climate,* **13,** 650–657.

Reichardt, J., S. Reichardt, A. Behrendt, and T. J. McGee, 2002a: Correlations among the optical properties of cirrus-cloud particles: Implications for spaceborne remote sensing. *Geophys. Res. Lett.,* **29,** 1668, doi:10.1029/2002GL014836.

Unauthenticated | Downloaded 04/29/24 02:28 PM UTC

——, ——, M. Hess, and T. J. McGee, 2002b: Correlations among the optical properties of cirrus-cloud particles: Microphysical interpretation. *J. Geophys. Res.,* **107,** 4562, doi:10.1029/2002JD002589.

Sakai, T., T. Nagai, M. Nakazato, Y. Mano, and T. Matsumura, 2003: Ice clouds and Asian dust studied with lidar measurements of particle extinction-to-backscatter ratio, particle depolarization, and water vapor mixing ratio over Tsukuba. *Appl. Opt.,* **42,** 7103–7116.

Sassen, K., 1991: The polarization lidar technique for cloud research: A review and current assessment. *Bull. Amer. Meteor. Soc.,* **72,** 1848–1866.

——, and S. Benson, 2001: A midlatitude cirrus cloud climatology from the Facility for Atmospheric Remote Sensing. Part II: Microphysical properties derived from lidar depolarization. *J. Atmos. Sci.,* **58,** 2103–2112.

——, and J. M. Comstock, 2001: A midlatitude cirrus cloud climatology from the facility for atmospheric remote sensing. Part III: Radiative properties. *J. Atmos. Sci.,* **58,** 2113–2127.

——, R. P. Benson, and J. D. Spinhirne, 2000: Tropical cirrus cloud properties derived from TOGA/COARE airborne polarization lidar. *Geophys. Res. Lett.,* **27,** 673–676.

——, W. P. Arnott, D.O'C. Starr, G. Mace, Z. Wang, and M. Poellet, 2003: Midlatitude cirrus clouds derived from Hurricane Nora: A case study with implications for ice crystal nucleation and shape. *J. Atmos. Sci.,* **60,** 873–891.

Schotland, R. M., K. Sassen, and R. J. Stone, 1971: Observations by lidar of linear depolarization ratios by hydrometeors. *J. Appl. Meteor.,* **10,** 1011–1017.

Shapiro, M. A., and A. J. Thorpe, 2004: THORPEX: A global atmospheric research program for the beginning of the 21st century. *WMO Bull.,* **53,** 222–226.

Solomon, S., D. Qin, M. Manning, Z. Chen, M. Marquis, K. B. Averyt, M. Tignor, and H. L. Miller, 2007: *Climate Change 2007: The Physical Science Basis.* Cambridge University Press, 996 pp.

Spinhirne, J. D., J. A. Reagan, and B. M. Herman, 1980: Vertical distribution of aerosol extinction cross section and inference of aerosol imaginary index in the troposphere by lidar technique. *J. Appl. Meteor.,* **19,** 426–438.

——, W. D. Hart, and D. L. Hlavka, 1996: Cirrus infrared parameters and shortwave reflectance relations from observations. *J. Atmos. Sci.,* **53,** 1438–1458.

——, S. P. Palm, W. D. Hart, D. L. Hlavka, and E. J. Welton, 2005: Cloud and aerosol measurements from GLAS: Overview and initial results. *Geophys. Res. Lett.,* **32,** L22S03, doi:10.1029/2005GL023507.

Stephens, G. L., 2005: Cloud feedbacks in the climate system: A critical review. *J. Climate,* **18,** 237–273.

Toon, O. B., and Coauthors, 2010: Planning, implementation, and first results of the Tropical Composition, Cloud and Climate Coupling Experiment (TC4). *J. Geophys. Res.,* **115,** D00J04, doi:10.1029/2009JD013073.

Vaughan, M. A., and Coauthors, 2009: Fully automated detection of cloud and aerosol layers in the CALIPSO lidar measurements. *J. Atmos. Oceanic Technol.,* **26,** 2034–2050.

——, Z. Liu, M. J. McGill, Y. Hu, and M. D. Obland, 2010: On the spectral dependence of backscatter from cirrus clouds: Assessing CALIOP's 1064 nm calibration assumptions using cloud physics lidar measurements. *J. Geophys. Res.,* **115,** D14206, doi:10.1029/2009JD013086.

Wang, Z., and K. Sassen, 2001: Cloud type and macrophysical property retrieval using multiple remote sensors. *J. Appl. Meteor.,* **40,** 1665–1682.

——, and ——, 2002: Cirrus cloud microphysical property retrieval using lidar and radar measurements. Part II: Midlatitude cirrus microphysical and radiative properties. *J. Atmos. Sci.,* **59,** 2291–2302.

Webster, P. J., and R. Lukas, 1992: TOGA COARE: The Coupled Ocean—Atmosphere Response Experiment. *Bull. Amer. Meteor. Soc.,* **73,** 1377–1416.

Whiteman, D. N., B. Demoz, and Z. Wang, 2004: Subtropical cirrus cloud extinction to backscatter ratios measured by Raman Lidar during CAMEX-3. *Geophys. Res. Lett.,* **31,** L12105, doi:10.1029/2004GL020003.

Winker, D. M., and Coauthors, 2009a: The CALIPSO mission: A global 3D view of aerosols and clouds. *Bull. Amer. Meteor. Soc.,* **91,** 1211–1229.

——, M. A. Vaughan, A. H. Omar, Y. Hu, K. A. Powell, Z. Liu, W. H. Hunt, and S. A. Young, 2009b: Overview of the CALIPSO mission and CALIOP data processing algorithms. *J. Atmos. Oceanic Technol.,* **26,** 1105–1119.

Yorks, J. E., M. McGill, S. Rodier, M. Vaughan, Y. Hu, and D. Hlavka, 2009: Radiative effects of African dust and smoke observed from Clouds and the Earth's Radiant Energy System (CERES) and Cloud-Aerosol Lidar with Orthogonal Polarization (CALIOP) data. *J. Geophys. Res.,* **114,** D00H04, doi:10.1029/2009JD012000.

Young, S. A., and M. A. Vaughan, 2009: The retrieval of profiles of particulate extinction from Cloud-Aerosol Lidar Infrared Pathfinder Satellite Observations (CALIPSO) data: Algorithm description. *J. Atmos. Oceanic Technol.,* **26,** 1105–1119.

——, D. M. Winker, M. A. Vaughan, Y. Hu and R. E. Kuehn, 2008: Part 4: Extinction retrieval algorithms. CALIOP Algorithm Theoretical Basis Doc. PC-SCI-202.01, 63 pp. [Available online at http://www-calipso.larc.nasa.gov/resources/pdfs/PC-SCI-202_Part4_v1.0.pdf.]

Unauthenticated | Downloaded 04/29/24 02:28 PM UTC